

Article

Application of Spectroscopic Characteristics of White Mica in Porphyry Tungsten Deposits: A Case Study Involving the Shimensi Deposit in Northern Jiangxi

Zhongxue Zhang ¹, Jingjing Dai ^{2,*}, Xianguang Wang ³, Zhenghua Hu ⁴, Xin Wan ³, Bo Peng ² and Minghai Fu ^{2,5}¹ School of Earth Sciences and Resources, China University of Geosciences, Beijing 100083, China² Ministry of Natural Resources Key Laboratory of Metallogeny and Mineral Assessment, Institute of Mineral Resources, Chinese Academy of Geological Sciences, Beijing 100037, China³ Jiangxi Mineral Resources Guarantee Service Center, Nanchang 330025, China⁴ Jiangxi Institute of Land and Space Investigation and Planning, Nanchang 330025, China⁵ Chinese Academy of Geological Sciences, China University of Geosciences, Beijing 100083, China

* Correspondence: qwerrosy@126.com; Tel.: +86-136-5135-7252

Abstract: Shortwave infrared (SWIR) technology is characterized by high efficiency and convenience and is widely used in the mineral exploration of porphyry, epithermal, and skarn types. However, studies on the SWIR spectral features of porphyry tungsten deposits are still lacking. The Dahutang tungsten deposit has reached an ultra large scale, characterized by the porphyry type. Based on the SWIR spectral features of white mica and its petrographic, geochemical, and Raman spectral features, this paper discusses the use of shortwave infrared and Raman spectral features and major and trace element contents in white mica for exploration of the Shimensi mine in Dahutang. The results showed that the SWIR wavelength of the single-frequency Al-O-H absorption peak position (Pos2200) of white micas in ore-bearing intrusions were over 2209 nm; the Raman shift of aluminium atom bridge-bonds (Al, O (br)) were mainly located between 410 and 420 cm^{-1} . The contents of Si, Fe, and Mg were relatively high; the contents of Al, Na, and K were low; and the variation of the Nb/Ta value reflected the magmatic evolution degree. The shift of Pos2200 of white mica showed a correlation with the Raman spectral features and contents of Si, Al, and other elements. This study shows that the SWIR spectral features of white mica were useful for further exploration of the Shimensi area in Dahutang and provided a potential tool for the exploration of porphyry tungsten deposits.

Keywords: porphyry tungsten deposit; white mica; shortwave infrared spectroscopy; Raman spectroscopy; EMPA; LA-ICP-MS



Citation: Zhang, Z.; Dai, J.; Wang, X.; Hu, Z.; Wan, X.; Peng, B.; Fu, M. Application of Spectroscopic Characteristics of White Mica in Porphyry Tungsten Deposits: A Case Study Involving the Shimensi Deposit in Northern Jiangxi. *Minerals* **2023**, *13*, 256. <https://doi.org/10.3390/min13020256>

Academic Editors: Nikita V. Chukanov, Zhenyu Chen and Fangyue Wang

Received: 5 December 2022

Revised: 12 January 2023

Accepted: 6 February 2023

Published: 11 February 2023



Copyright: © 2023 by the authors. Licensee MDPI, Basel, Switzerland. This article is an open access article distributed under the terms and conditions of the Creative Commons Attribution (CC BY) license (<https://creativecommons.org/licenses/by/4.0/>).

1. Introduction

Isomorphous substitution results in the elemental content variation in minerals of the same type. These minerals with multiple element combinations record the formation process and characteristics of rocks and deposits composed of minerals, which is significant for ore exploration. At the same time, the elemental changes caused by isomorphous substitution can also result in a shift of the spectral feature [1–3]. Mineral spectral measurement technology has developed rapidly in recent years and is widely used to extract mineralization information on altered minerals in ore deposits [4–7]. Compared with other factors that are indicative for mineralization, mineral spectral technology is more rapid and convenient and has good application prospects.

Shortwave infrared (SWIR) technology is a hyperspectral technology, and its band range (1100–2500 nm) has a strong response capability for molecular vibrations of hydrated and hydroxyl-bearing minerals (such as clay minerals, carbonates, and partially hydrated sulphates) with combined frequency and frequency doubling [8,9]. White mica is a layered

silicate mineral, and the diagnostic absorption of SWIR spectra of white mica is the single-frequency Al-O-H absorption peak. The band shifts regularly with the Al content. As a kind of common rock-forming mineral and alteration mineral, the changes in white mica SWIR spectral features are widely used in prospecting and in the exploration of porphyry copper deposits, epithermal deposits, skarn deposits, and other types of deposits. Currently, some studies have shown that higher wavelength (Si-rich) white mica is closely related to the mineralization in the Canadian Malartic gold deposit, Kanowna Belle gold deposit, and Laowangou Au deposit, while shorter wavelength white mica in Pebble Cu-Au-Mo porphyry, the Sunrise Dam gold deposit, and Chating Cu-Au deposit indicates the location of the orebody. Therefore, the shift of Pos2200 in white mica indicating mineralization in various types of deposits is different [10–14]. In porphyry tungsten deposits, studies on the SWIR spectral features of white mica and its prospecting significance are lacking.

Porphyry tungsten deposits are among the important tungsten deposits in the world, they are mainly distributed in the circum-Pacific metallogenic belt and the Alps-Himalayan metallogenic belt, and they occur in magmatic arc, intraplate, and continental collisions and other settings [15]. Among them, the Dahutang ore region in northern Jiangxi is one of the largest porphyry tungsten polymetallic ore fields in the world. The Shimensi mine is located in the northern Dahutang ore region. It is also a world-class tungsten deposit, containing estimated reserves of 0.74 Mt WO_3 (average grade is 0.195%), 0.4 Mt Cu, and 28 Kt Mo [16,17].

White mica is used as an indicator mineral for the Shimensi tungsten mine, and the relationship between white mica and mineralization is discussed according to the SWIR spectra, microlaser Raman spectra, petrography, and geochemical features of the white mica to provide guidance for the exploration and prospecting of porphyry tungsten deposits.

2. Regional and Deposit Geology

The Dahutang ore region is located at the junction of Wuning, Xiushui, and Jing'an. Its geographical coordinates are $114^{\circ}55'44.99''$ – $114^{\circ}57'09.29''$ E, and $28^{\circ}52'51.00''$ – $28^{\circ}56'47.36''$ N, covering an area of about 13 km² [18].

The Dahutang area is located in the middle of the Jiangnan orogenic belt, which is an important tungsten polymetallic metallogenic concentration [19,20]. The proven tungsten resources in the Jiangnan tungsten ore belt are nearly 6.06 Mt, of which the Dahutang tungsten resources are 1.1 Mt [19,20]. The exposed stratum in Dahutang ore region is the Neoproterozoic Shuangqiaoshan Group, which is a deep-sea volcanic clastic sedimentary formation formed in a fault depression environment. The lithology is dominated by greyish green greywacke and slate interbedding, with a little complex metamorphic conglomerate [16]. The intrusion includes Neoproterozoic biotite granodiorite and Mesozoic granite, and the latter is related to the genesis of W, Cu, and Sn deposits in this area [21]. Tungsten polymetallic deposits, such as Shimensi, Shiweidong, Kunshan, Dalingshang, and Dawutang are distributed in the ore region [22].

The Shimensi mine is an important part of the Dahutang ore region, and it is located in the northern Dahutang ore region [23]. The exposed stratum of Shimensi is only Quaternary residual soil, and the bedrock is Neoproterozoic biotite granodiorite and acid plutonic to hypabyssal Yanshanian granite [16,24]. There is multistage magmatic activity in the region, mainly from the Jinningian magmatism and Yanshanian magmatism [22]. The Jinningian biotite granodiorite, as a batholith in the ore region, is a main ore-bearing wall rock [20]. There were many magmatic intrusions in the Yanshanian magmatism. The coarse-grained porphyritic biotite granite (CPBG), fine-grained porphyritic biotite granite (FPBG), fine-grained biotite granite (FBG), and biotite granite porphyry (BGP) of the Yanshanian magmatism were developed as stocks, nodules, and rock branches and some of them intruded into the Jinningian biotite granodiorite batholith. They are important ore-forming parent rocks in the region (Figure 1) [25]. The folds in the region are mainly the eastward extension of the Jinglin-Caobingchang secondary anticline of the Jiuling complex fold, which is NEE-trending. The regional faults are mainly NE, NE-

NNE, NW, and NS-trending. The main ore-controlling faults are the Shimensi fault and Xiangguoshan-Dahutang-Shiweidong basement fault [25,26]. Shimensi porphyry tungsten deposits mainly form veinlet-disseminated scheelite mineralization in the internal and external contact zones of intrusions [27]. The main ore minerals are scheelite, wolframite, chalcopyrite, molybdenite, etc. Scheelite is usually crosscut by late sulphides, including chalcopyrite, pyrite, and molybdenite. The gangue minerals are quartz, feldspar, chlorite, fluorite, and a small amount of white mica [25]. The alteration types can be divided into potassium feldspar, biotitization, greisetization, chloritization, fluoritization, and silicification. Greisetization and sericitization are closely related to scheelite mineralization. The alteration and mineralization have a positive correlation, so white mica can be used as a key indicator for exploration [16].

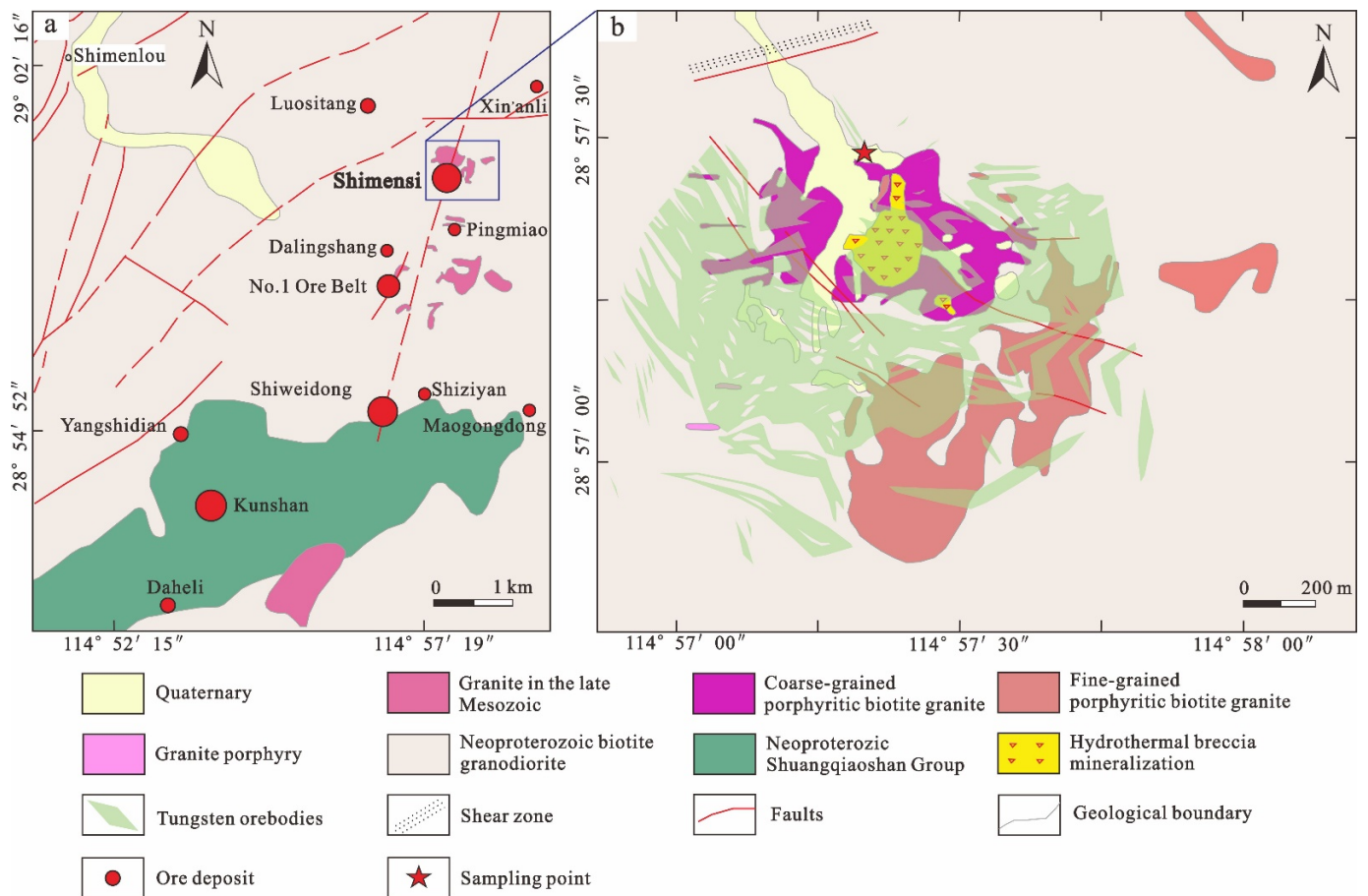


Figure 1. (a) Simplified geological map of the Dahutang ore field. (b) Geological map of the Shimensi mine (modified from [17]).

3. Sampling and Methods

3.1. Sampling

It is necessary to collect and record samples of ore-bearing intrusions containing scheelite and barren intrusions in the Shimensi mining area. The orebodies in the study area were mainly distributed in the inner–outer contact zone and the fissures of the wall rocks. We can distinguish whether the rock mass contains scheelite by using the characteristic of scheelite which appears sky-blue under ultraviolet light. Thirty-eight samples were collected by combining the known geological and metallogenic conditions and characteristic of scheelite and 32 petrographic thin sections were made in the Shimensi mine. All samples were collected from the same pit, whose central coordinates are 114°57'20" E, 28°57'28" N (Figure 1).

3.2. Shortwave Infrared Spectroscopy

FieldSpec4, developed by the American ASD (Analytical Spectral Devices, Inc.) company, was used for SWIR data acquisition. The spectral range was 350–2500 nm. The spectral resolution of the SWIR instrument was 3 nm over the range of 350–700 nm and 6 nm for the range above of 700 nm. The spectral sampling interval of the FieldSpec4 (ASD) instrument was 1.4 nm at 350–1050 nm and 2 nm at 1000–2500 nm. Prior to the SWIR spectra measurements, the core was cleaned, wiped and dried. During the measurement, the surface of the sample should be fresh, smooth, and flat. The SWIR spectra measurement was carried out on the rock hand specimen. During the test, the instrument was preheated first, and then calibrated. The sample could be measured when the spectrum was at the same level as 1. The contact probe was used to test the white mica concentration area. The probe had a built-in light source, and the front aperture of the probe was fitted with the test surface to reduce the interference of the external light and ensure the consistency of the test conditions. During analysis, the SWIR spectrum was derived from the spectrometer, and The Spectral Geologist (TSG) was used to identify the mineral species and extract the location of the white mica characteristic absorption valley.

3.3. Micro-Raman Spectroscopy

The micro-Raman spectroscopy test was carried out in the Environmental Mineralogy Laboratory of Peking University. The test instrument was an inVia reflex spectrometer from the Renishaw company in the UK. The excitation wavelength was 532 nm; the laser emission power was 50 mW; the slit width was 65 μm for the solid-state laser, the Leica objective lens was 50 times; and the numerical aperture was 0.75. A static grating was used in the experiments. The single scanning time of the sample was 30 s; the cumulative number of scans was 25; the spectral resolution was 1 cm^{-1} ; and the data acquisition range was 50–1300 cm^{-1} .

3.4. Electron Microprobe Analysis (EMPA)

Electron microprobe analyses were completed in the Electron Microprobe Laboratory of the Institute of Mineral Resources, Chinese Academy of Geological Sciences. The experimental instrument was a JXA-8230 model made by JEOL, Japan. The element test conditions involved an acceleration voltage of 15 kV, excitation current of 20 nA, and electron beam diameter of 1–5 μm . Natural samples and synthetic oxides were used as standard samples in the testing process, including quartz (Si), jadeite (Al), plagioclase (Na), pyrope (Mg), hematite (Fe), manganese oxide (Mn), apatite (Ca, P), K-feldspar (K), phlogopite (F), halite (Cl), rutile (Ti), celestine (Sr), lithium niobate (Nb), lithium tantalate (Ta), and cobalt (Co). The measured data were corrected using the ZAF method.

3.5. Laser Ablation Inductively Coupled Plasma Mass Spectrometry (LA-ICP-MS)

Trace elements in the white micas were measured by LA-ICP-MS at Guangzhou TuoYan Analytical Technology Co., Ltd., Guangzhou, China. Laser sampling was performed using an NWR 193 laser ablation system. An iCAP RQ ICP-MS instrument was used to acquire ion-signal intensities. Helium was applied as the carrier gas. Argon was used as the make-up gas and mixed with the carrier gas via a Y-connector before entering the ICP. The spot size and frequency of the laser were set to 30 μm and 6 Hz, respectively, in this study. The energy was 3.5 J/cm^2 . Glass NIST610 and NIST 612 standards [28] were used as external standards for trace element calibration. Each analysis incorporated a background acquisition of approximately 30 s followed by 40 s of data acquisition from the sample. Excel-based software ICPMSDataCal [29] was used to perform the off-line selection and integration of the background and analysed signals, the time-drift correction, and trace element analyses.

4. Results

4.1. Mineral Characteristics

The porphyry tungsten deposit in Shimensi is mainly distributed in the wall rock fissures of the Jinningian biotite granodiorite and the contact zone of the Jinningian biotite granodiorite and Yanshanian granite. Generally, the mineral grains in the barren intrusions are distinct. The boundary is relatively clear, and there are no obvious alteration characteristics. Alteration minerals were developed in ore-bearing intrusions, and quartz veins are often developed.

The types of white micas in ore-bearing intrusions and barren intrusions are distinct under the microscope, mainly including: flaky primary white micas with a slightly rough surface and local deformation, and fine and straight continuous cleavage can be seen on the parallel to or oblique to the C-axis (Figure 2a); Radiolitic or bamboo leaf white micas, which are allotriomorphic and have a bright interference colour (Figure 2b); White micas with fine-scale aggregates, which are mainly formed by feldspar alteration, are irregularly distributed on the surface of feldspar, or feldspar completely eroded into fine scaly aggregates of white micas (Figure 2c); White micas with an alteration feature replaced from biotite is distributed along the cleavage and margin of biotite (Figure 2d). In ore-bearing intrusions, radiolitic or bamboo leaf white micas, fine-scale aggregate white micas, and white micas formed by metasomatic biotite are mainly developed. In the barren intrusions, it is mainly flaky primary white micas and a small quantity of fine-scale aggregate white micas.

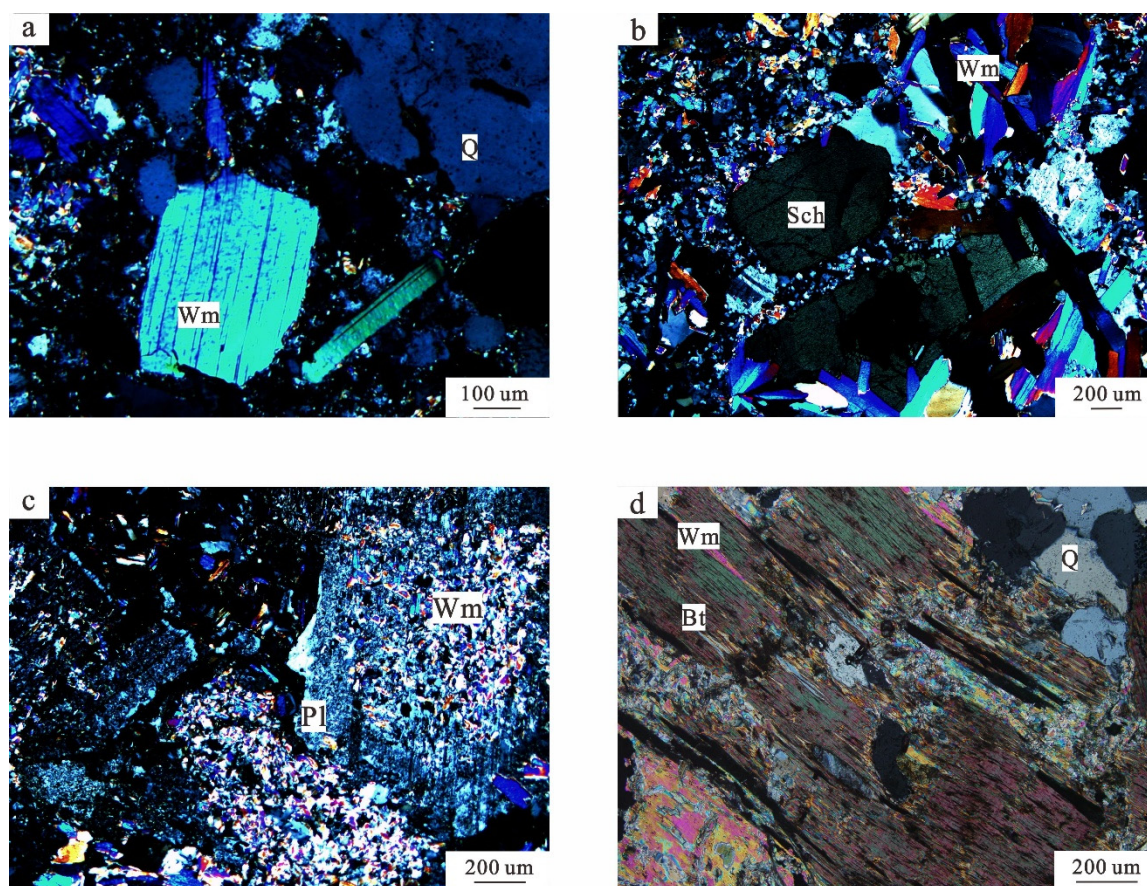


Figure 2. Photomicrographs of different types of white mica. (a) Flaky primary white micas; (b) White mica symbiotic with tungsten ore; (c) Feldspar-altered secondary white micas associated with scheelite; (d) White micas metasomatized by biotite (Bt—Biotite; Pl—plagioclase; Q—quartz; Sch—scheelite; Wm—white mica).

4.2. Spectral Characteristics

4.2.1. SWIR Spectra of White Mica

The SWIR spectra of white micas from the study area had obvious absorption peaks at 1408, 1910, 2200, 2348, and 2442 nm and were similar to the SWIR spectrum curve of standard white mica. Based on the measured shift of Pos2200 of white micas from the study area, they can be divided into two types of white mica (Figure 3a). One was characterized by a higher Pos2200 value with a range of 2209–2216 nm (Figure 3b). According to the characteristics of SWIR spectra, these white micas, which mainly exist in the ore-bearing intrusions, are more similar to phengite. The other type of white mica was ordinary white mica with Pos2200 at 2198–2208 nm (Figure 3b), and they are mainly located in the barren intrusions. The shift Pos2200 for white micas in the ore-bearing intrusions was inclined toward the high wavelength direction, while for the white mica in barren intrusions, it was inclined toward the low wavelength direction.

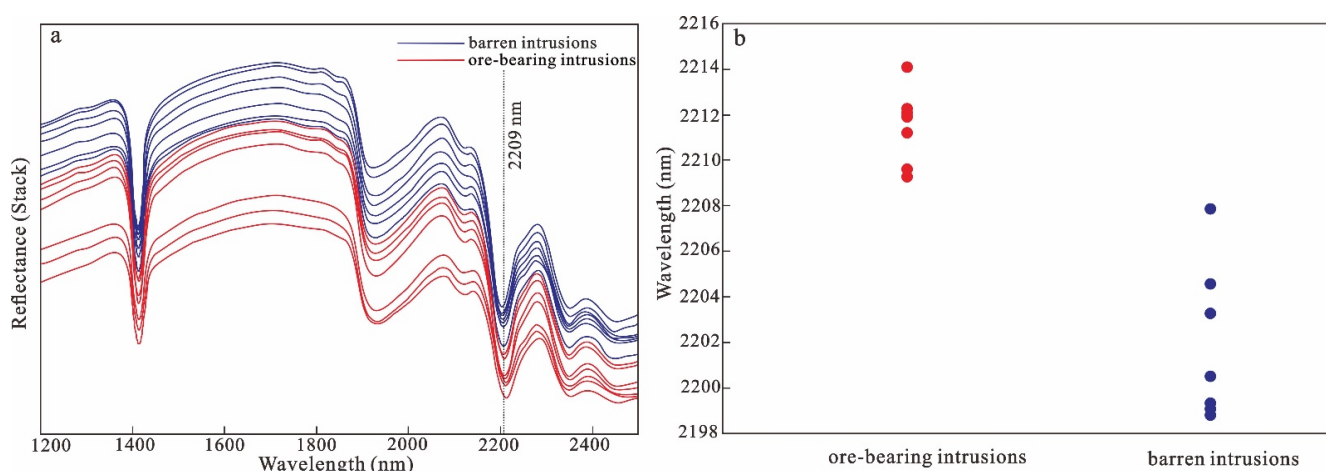


Figure 3. (a) SWIR spectra of white micas from ore-bearing intrusions and barren intrusions; (b) Statistical diagram of SWIR spectra absorption feature wavelengths (2198–2216 nm) for white micas from ore-bearing intrusions and barren intrusions.

4.2.2. Raman Spectral Characteristics of White Mica

The micro-Raman spectra of white micas from different intrusions in the study area are shown in Figure 4. The main Raman peaks were at 261, 408, 701 cm^{-1} , etc. Previous studies suggested that the mineral does not change its crystal structure space group, but chemical substitution will change the bond lengths and bond angles of the mineral lattice and result in a change in the Raman shift. The Raman peaks in the spectral region $<600 \text{ cm}^{-1}$ arise from a complex set of translational motions of cations in octahedral sites and in interlayer sites relative to the SiO_4 groups in tetrahedral layers, the oxygens, and the OH groups. The Raman peak at 261 cm^{-1} was mainly caused by lattice vibrations, and the Raman peak at 408 cm^{-1} was related to the aluminium atom bridge-bonds (Al, O (br)) (Figure 4a). The Raman peaks in the spectral region 800–600 cm^{-1} were attributed to the vibrational modes of $\text{Si-O}_b\text{-Si}$ bonds (O_b = bridging oxygen), which connect the SiO_4 tetrahedra that make up a layer. The strong Raman peak at about 701 cm^{-1} is related to stretching vibrations of the AlO_4 tetrahedra. The Raman peaks in the spectral region 1150–800 cm^{-1} arise from the stretching mode of the Si-O_{nb} bond (O_{nb} = non-bridging oxygen) in SiO_4 tetrahedra [30–32]. The Raman shift at 261, 408, 701 cm^{-1} for white micas from the ore-bearing intrusions, respectively, are mainly between 263–264, 410–420, and 701–704 cm^{-1} , while those for white mica from the barren intrusions, respectively, are 263–264, 406–413, and 701–703 cm^{-1} . In this study area, the Raman peak positions at 408 cm^{-1} for white micas from ore-bearing intrusions and barren intrusions had obvious differences (Figure 4b).

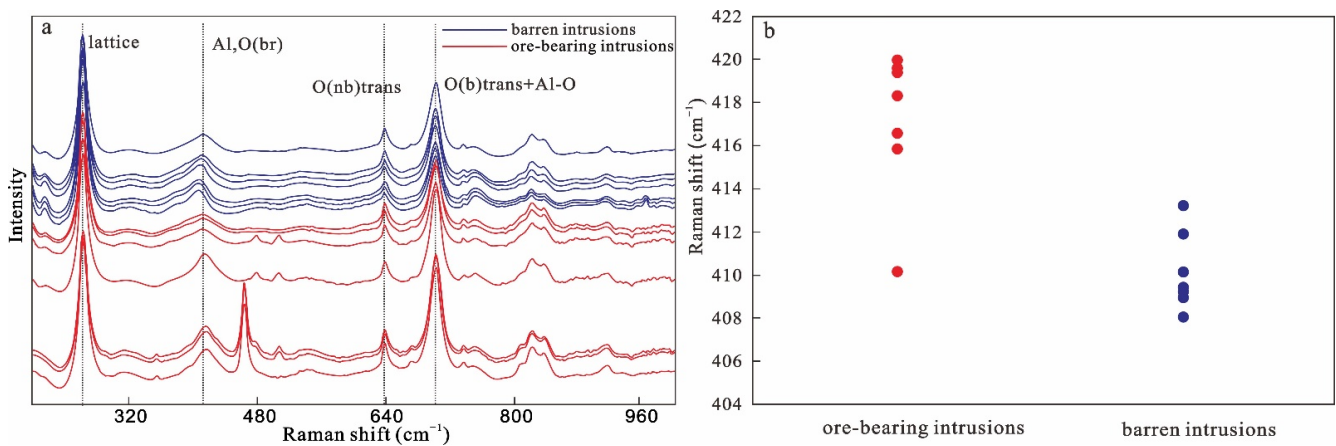


Figure 4. (a) Micro-Raman spectra of white mica from ore-bearing intrusions and barren intrusions; (b) The Raman shift of aluminium atom bridge-bonds (Al, O (br)) for white mica from ore-bearing intrusions and barren intrusions.

4.3. Geochemical Characteristics of White Mica

4.3.1. Major Elements

White micas show variable concentration ranges (in wt%) of SiO₂, 45.96–48.66; Al₂O₃, 30.00–37.49; FeO, 0.71–3.01; MgO, 0.13–2.72; Na₂O, 0.17–0.45; and K₂O, 6.10–9.30. On the whole, white mica from the whole study area showed high Si content and low Al content. Among the samples, white mica from different intrusions also showed obvious differences in the contents of major elements. The SiO₂ content of white mica from the barren intrusions was 45.96–46.77%, with an average value of 46.43%. The Al₂O₃ content in white mica was 34.82–37.49%, and the average value was 36.03%. The FeO content in white mica was 0.71–2.00%, and the average value was 1.34%. The MgO content in white mica was 0.13–0.85%, and the average value was 0.51%. The Na₂O content in white mica was 0.30–0.45%, and the average value was 0.36%. The K₂O content in white mica was 7.16–9.30%, and the average value was 8.46%. In the ore-bearing intrusions, the SiO₂ content in white mica was 47.51–48.66%, with an average value of 48.21%; the content of Al₂O₃ was 30.00–32.79%, with an average value of 31.49%; the content of FeO was 2.22–3.01%, with an average value of 2.68%; the content of MgO was 1.16–2.72%, with an average value of 1.85%; the content of Na₂O was 0.17–0.23%, with an average value of 0.21%; and the content of K₂O was 6.10–8.44%, with an average value of 6.92%. According to these results, the white mica from the ore-bearing intrusions had higher SiO₂ contents, lower Al₂O₃ contents, higher FeO contents, higher MgO contents, and lower Na₂O and K₂O contents compared to the white mica from the barren intrusions (Table 1).

Table 1. Results of the electron microprobe analysis of white micas.

Sample	Barren Intrusions								Ore-Bearing Intrusions					
	S1	S2	S3	S4	S5	S6	S7	S8	S9	S10	S11	S12	S13	S14
	<i>w(B)/%</i>													
SiO ₂	46.31	46.31	45.96	46.70	46.37	46.57	46.77	47.51	47.90	48.66	48.36	48.14	48.26	48.64
TiO ₂	0.47	-	0.07	0.52	0.31	0.03	0.37	0.58	0.60	0.47	0.19	0.30	0.50	0.42
Al ₂ O ₃	36.27	36.25	36.24	35.53	35.60	37.49	34.82	31.49	30.93	3.00	32.17	32.48	30.58	32.79
FeO	1.17	0.71	1.37	1.48	2.00	1.19	1.47	2.90	2.63	2.88	2.60	3.01	2.51	2.22
MnO	0.02	-	0.07	0.09	0.07	0.05	-	0.04	0.05	0.08	0.13	0.09	0.07	0.09
MgO	0.54	0.47	0.42	0.54	0.60	0.13	0.85	1.84	1.85	2.72	1.61	1.41	2.39	1.16
CaO	-	-	-	-	-	-	-	0.01	-	0.03	0.01	-	0.01	-
Na ₂ O	0.39	0.45	0.41	0.30	0.34	0.30	0.31	0.23	0.21	0.17	0.21	0.23	0.20	0.19
K ₂ O	8.93	8.89	9.23	7.86	7.16	7.86	9.30	7.41	8.44	6.72	6.10	6.16	6.47	7.16
P ₂ O ₅	0.03	0.05	-	0.02	0.01	0.02	0.01	-	-	-	0.01	-	-	-
CoO	1.09	0.89	0.81	1.33	1.26	1.18	0.93	1.22	0.62	0.89	1.14	0.49	0.66	1.00

Table 1. Cont.

Sample	Barren Intrusions									Ore-Bearing Intrusions				
	S1	S2	S3	S4	S5	S6	S7	S8	S9	S10	S11	S12	S13	S14
Cl	0.01	0.01	0.01	-	-	-	-	-	-	0.01	-	0.02	0.02	0.01
F	0.02	0.21	0.19	1.17	1.34	0.80	0.50	0.80	0.87	0.87	1.02	0.83	1.19	0.62
Total	95.25	94.24	94.78	95.54	95.06	95.62	95.33	94.03	94.10	93.50	93.55	93.16	92.86	94.30
Number of ions on the basis of 11O														
Si	3.07	3.09	3.06	3.11	3.10	3.08	3.13	3.22	3.23	3.29	3.26	3.24	3.29	3.26
Ti	0.02			0.03	0.02		0.02	0.03	0.03	0.02	0.01	0.01	0.03	0.02
Al	2.83	2.85	2.85	2.80	2.80	2.92	2.75	2.52	2.46	2.39	2.56	2.58	2.46	2.59
Fe	0.06	0.04	0.08	0.08	0.11	0.07	0.08	0.16	0.15	0.16	0.15	0.17	0.14	0.12
Mn											0.01			
Mg	0.05	0.05	0.04	0.05	0.06	0.01	0.09	0.19	0.19	0.27	0.16	0.14	0.24	0.12
Ca														
Na	0.05	0.06	0.05	0.04	0.04	0.04	0.04	0.03	0.03	0.02	0.03	0.03	0.03	0.02
K	0.75	0.76	0.78	0.67	0.61	0.66	0.79	0.64	0.73	0.58	0.52	0.53	0.56	0.61
P														
Al ^{IV}	0.93	0.91	0.94	0.89	0.90	0.92	0.87	0.78	0.77	0.71	0.74	0.76	0.71	0.74
Al ^{VI}	1.90	1.94	1.91	1.91	1.90	2.00	1.88	1.74	1.69	1.68	1.82	1.82	1.75	1.84

Note: - : below detection limit.

4.3.2. Trace Elements

Among the trace elements of white micas in the study area, the overall content of rare earth elements is low, and most of them are below the detection limit (Table 2). The Nb/Ta ratio of white mica generally varies with the degree of magmatic evolution, and normally decreases with an increasing evolution trend [33]. The Nb/Ta value of white micas for the ore-bearing intrusions (1.72–14.06) in the study area were relatively smaller than the barren intrusions (12.78–23.08), indicating that ore-bearing intrusions may have a higher magmatic evolution (Figure 5).

Table 2. Results of the LA-ICP-MS of white micas (ppm).

Sample	Barren Intrusions									Ore-Bearing Intrusions				
	S1	S2	S3	S4	S5	S6	S7	S8	S9	S10	S11	S12	S13	S14
La	-	0.01	-	-	-	0.01	-	-	-	-	0.04	-	-	0.01
Ce	-	-	-	0.07	0.02	-	0.02	0.01	0.01	-	0.11	0.01	-	0.01
Pr	-	-	-	-	-	-	-	-	-	-	0.03	-	-	0.01
Nd	-	-	-	-	-	0.04	-	-	-	-	0.13	-	-	-
Sm	-	-	-	-	-	-	-	-	-	-	-	0.05	-	0.04
Eu	0.08	0.15	0.14	0.01	0.04	0.09	0.07	0.03	0.10	0.03	0.15	0.17	0.05	0.02
Gd	0.28	0.11	0.81	0.24	0.74	0.80	0.20	0.41	0.27	0.18	0.55	0.71	0.15	0.29
Tb	-	-	-	-	-	-	-	-	-	-	-	-	-	-
Dy	-	-	-	0.02	-	-	-	-	-	-	0.03	-	-	0.02
Ho	0.01	-	-	-	-	-	0.01	-	-	-	0.01	-	-	-
Er	-	-	-	-	-	-	-	-	-	-	-	0.03	-	0.02
Tm	-	-	-	-	0.01	-	-	0.01	-	-	-	-	0.00	-
Yb	-	0.03	-	-	0.02	0.05	0.02	0.02	-	0.03	0.05	0.04	-	0.02
Lu	0.01	-	-	0.01	-	0.02	0.01	0.03	-	0.01	-	0.01	-	0.03
LREE	0.08	0.17	0.14	0.08	0.06	0.14	0.09	0.04	0.11	0.03	0.46	0.22	0.05	0.09
HREE	0.29	0.14	0.81	0.27	0.77	0.86	0.24	0.47	0.27	0.21	0.63	0.80	0.16	0.37
LREE/ HREE	0.27	1.22	0.17	0.29	0.08	0.16	0.37	0.09	0.42	0.13	0.73	0.28	0.34	0.23
Rb	214.44	196.75	234.16	1872.24	394.21	842.40	794.57	227.17	1300.56	1184.39	1412.60	1963.55	1702.36	284.04
Ba	1685.14	249.50	1364.43	546.13	1270.41	988.89	937.85	404.46	388.34	609.46	995.85	320.61	507.22	397.96
Sr	7.36	4.11	6.76	9.21	6.64	6.89	8.57	5.85	8.76	5.59	18.49	16.34	5.51	4.71
Hf	0.04	0.04	0.08	0.05	0.12	0.11	0.08	0.02	0.02	0.05	0.07	0.02	0.02	0.02
Ta	1.33	0.10	0.35	0.36	0.37	0.56	0.56	0.19	0.28	0.31	0.27	0.35	0.21	0.07
W	58.57	4.14	3.81	52.72	13.01	41.00	30.94	0.95	24.31	13.11	38.28	33.59	18.01	3.99
Tl	0.60	0.53	0.60	8.20	1.28	3.67	2.74	0.57	5.56	4.96	6.44	9.43	8.16	0.62
Cs	11.93	4.71	7.26	777.48	141.20	515.85	317.06	5.64	691.72	713.52	260.08	673.59	458.40	12.58
Nb	18.61	2.36	4.45	4.69	7.15	8.03	8.36	0.33	2.59	2.35	2.05	4.87	2.52	0.37

Table 2. Cont.

Sample	Barren Intrusions									Ore-Bearing Intrusions				
	S1	S2	S3	S4	S5	S6	S7	S8	S9	S10	S11	S12	S13	S14
V	410.14	16.50	210.55	56.93	206.00	157.04	171.24	6.91	40.18	54.47	92.41	169.23	200.57	8.65
Li	165.38	188.24	197.73	1532.19	359.07	1189.04	631.15	260.58	204.12	389.80	1662.50	1626.17	1887.22	205.29
Cr	413.47	-	-	-	28.72	19.39	23.02	3.22	103.72	4.03	-	514.85	440.38	101.90
Sc	111.59	5.67	19.87	10.14	54.88	20.07	31.87	8.07	5.98	7.60	12.61	47.22	46.77	9.63
Co	1.41	1.79	2.63	8.27	2.58	2.46	2.07	-	0.34	0.32	1.69	2.90	1.44	1.01
Ni	2.55	3.57	4.97	11.92	8.84	7.79	4.92	0.80	0.61	0.59	1.56	6.23	1.60	1.87
Cu	0.78	0.76	0.61	0.44	-	0.25	0.63	0.57	0.84	1.50	0.41	0.48	0.48	3.13
Zn	11.85	12.81	15.34	116.73	26.52	94.43	48.77	18.58	43.03	39.78	70.50	114.59	98.60	21.37
Nb/Ta	14.00	23.08	12.78	13.00	19.17	14.48	15.03	1.72	9.16	7.72	7.69	14.06	11.90	5.40

Note: -: below detection limit.

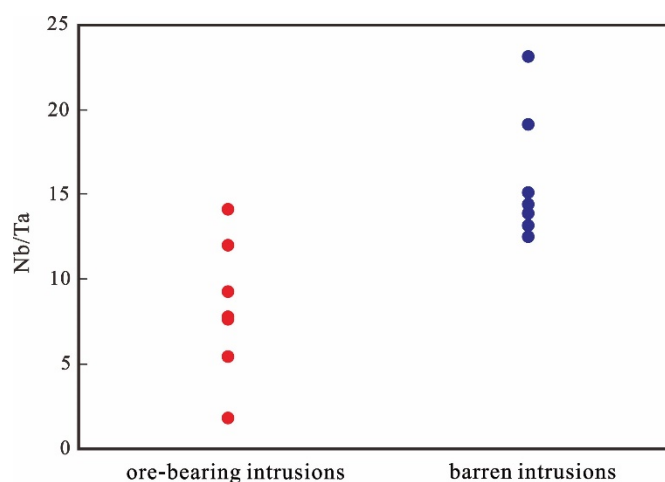


Figure 5. Nb/Ta input point diagram for ore-bearing intrusions and barren intrusions.

5. Discussion

5.1. Relationship between SWIR Spectra, Micro-Raman Spectra, and the Chemistry Characteristic of White Mica

5.1.1. Relationship between Spectral Characteristics and the Chemistry of White Mica

The changes in the spectral absorption peaks for minerals are usually related to replacement of the elements. The contents of Si, Al, Fe, Mg, Na, K, and other major elements in white micas from ore-bearing intrusions and barren intrusions were quite different. The average formula of white micas from the barren intrusions (Table 1) is $K_{0.72}Na_{0.05}Fe_{0.07}Mg_{0.05}Al_{1.92}(Si_{3.09}Al_{0.91})O_{10}(OH)_2$, and the average formula of white micas from the ore-bearing intrusions (Table 1) is $K_{0.6}Na_{0.03}Fe_{0.15}Mg_{0.19}Al_{1.76}(Si_{3.26}Al_{0.74})O_{10}(OH)_2$. Compared with the standard chemical formula of muscovite ($KAl_2(AlSi_3)O_{10}(OH)_2$), white micas from ore-bearing intrusions contain more phengitic composition. Previous studies have shown that octahedra in white mica crystals are mainly occupied by Al^{VI} , Fe, and Mg, and there is a mutual displacement relationship; the tetrahedral positions are mainly occupied by Al^{IV} and Si, and there is a displacement relationship [34,35]. The results of this study show that contents of Si, Fe, and Mg in white micas from the ore-bearing intrusions were higher than the barren samples, and the contents of Al (Al^{VI} and Al^{IV}), Na, and K were lower (Table 1). The shift of Pos2200 in white micas from the ore-bearing intrusions was inclined towards the high wavelength direction, while the characteristics of white micas from the barren intrusions were opposite. The analysis shows (Figure 6) that the shift of Pos2200 in white mica is positively correlated with Si, Fe, Mg, and Si:Al ratio while it is negatively correlated with Al, K, and Na, with a high degree of correlation. Therefore, the higher the Al content and the lower the Si content in white micas, the more the Al-O-H absorption peak shifts in the low wavelength direction.

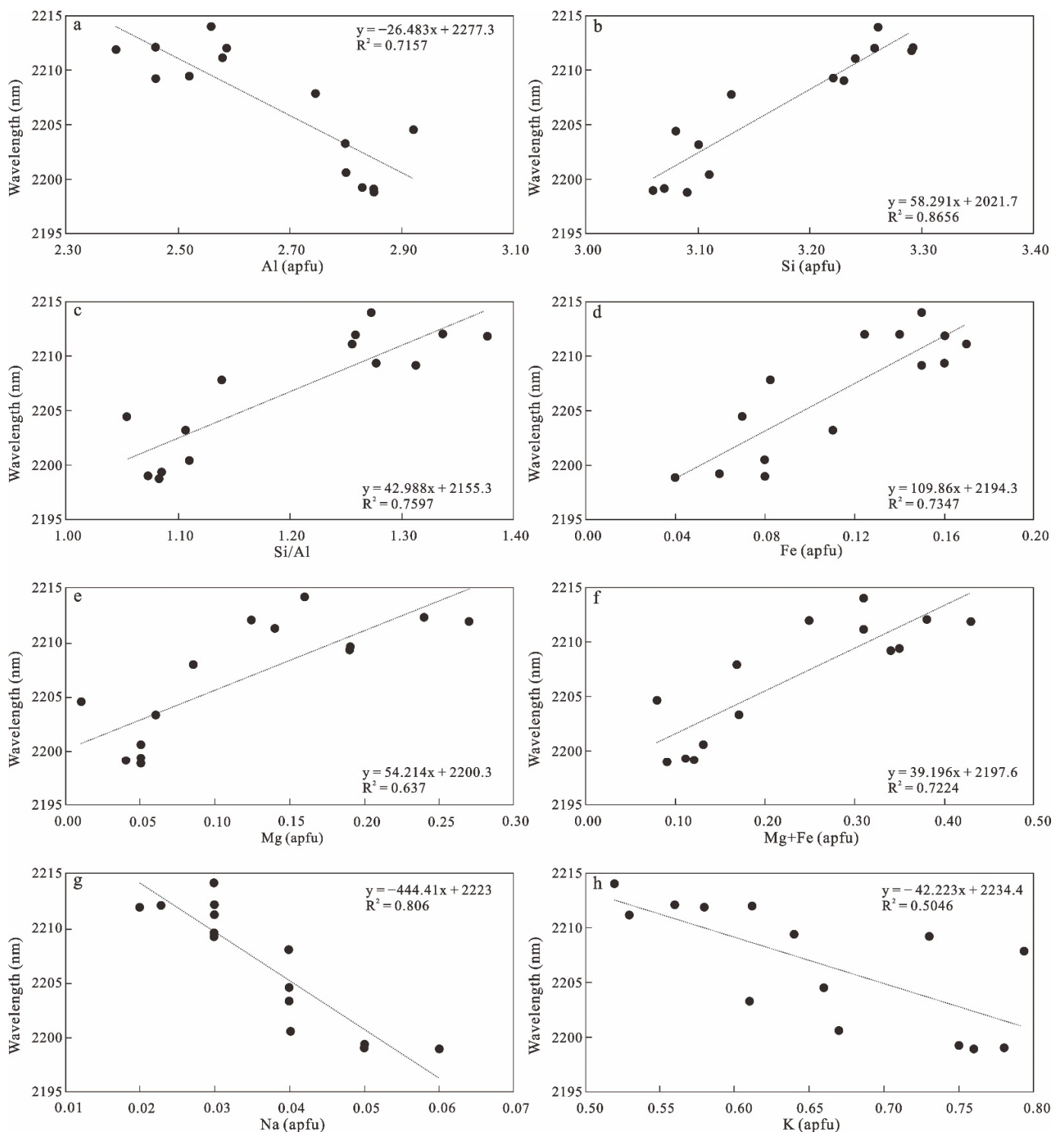


Figure 6. Binary diagram of the SWIR spectra (Pos 2200) for the Shimensi white micas vs. (a) Al; (b) Si; (c) Si/Al; (d) Fe; (e) Mg; (f) Mg + Fe; (g) Na; (h) K.

The shift of the Raman peak at 408 cm^{-1} is also closely related to its elemental content. In ore-bearing intrusions, white micas have high Raman shift values ($410\text{--}420\text{ cm}^{-1}$), Si, Mg, and Fe contents but low Al, K, and Na contents. The opposite is found in barren intrusions. The correlation between Raman shifts ($406\text{--}420\text{ cm}^{-1}$) of white mica and the elemental content follows the same trend as the SWIR spectra ($2198\text{--}2216\text{ nm}$), with positive

correlations with Si, Fe, and Mg and negative correlations with Al, K, and Na, but to a slightly lower degree (Figure 7).

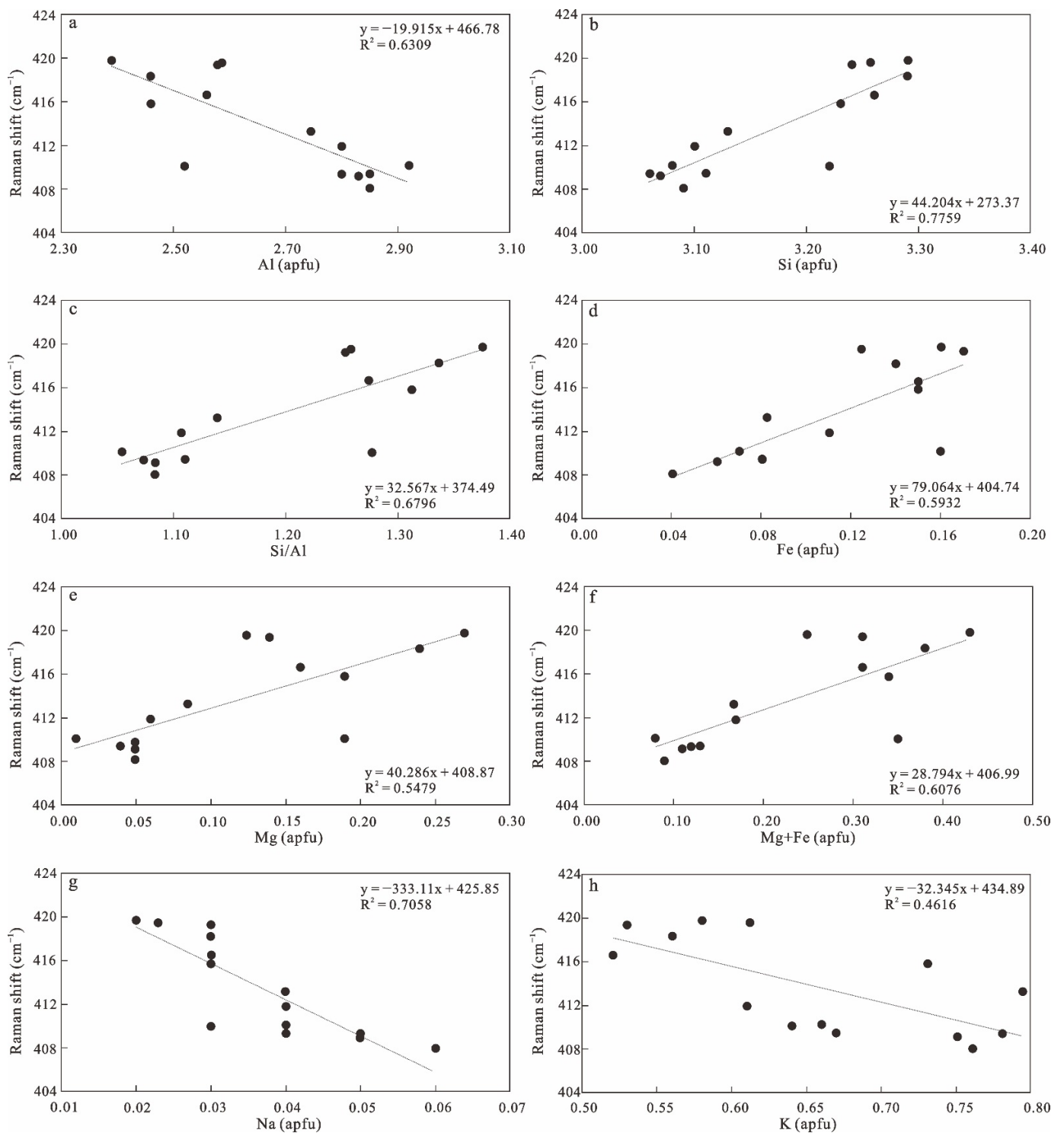


Figure 7. Binary diagram of Raman shift (Al, O (br)) for the Shimensi white micas vs. (a) Al; (b) Si; (c) Si/Al; (d) Fe; (e) Mg; (f) Mg + Fe; (g) Na; (h) K.

In addition, trace elements were also related to the shift of Pos2200 in white micas. There was a moderate negative correlation between the Nb/Ta ratio and the Pos2200 value in white mica, with a correlation coefficient of about 0.64 (Figure 8a). In connection with the

above research results, it was found that the ore-bearing intrusions have a higher magmatic evolution, because tungsten is a highly incompatible element, the strong magmatic evolution process is more conducive to tungsten enrichment and mineralization. In this process, phengite with characteristic absorption biased to the long-wave has been produced. The study showed that the correlation between trace elements and the Pos2200 value in white mica is lower than that between major elements and the Pos2200 value in white mica, and the major elements have a greater influence on the SWIR spectrum of white mica.

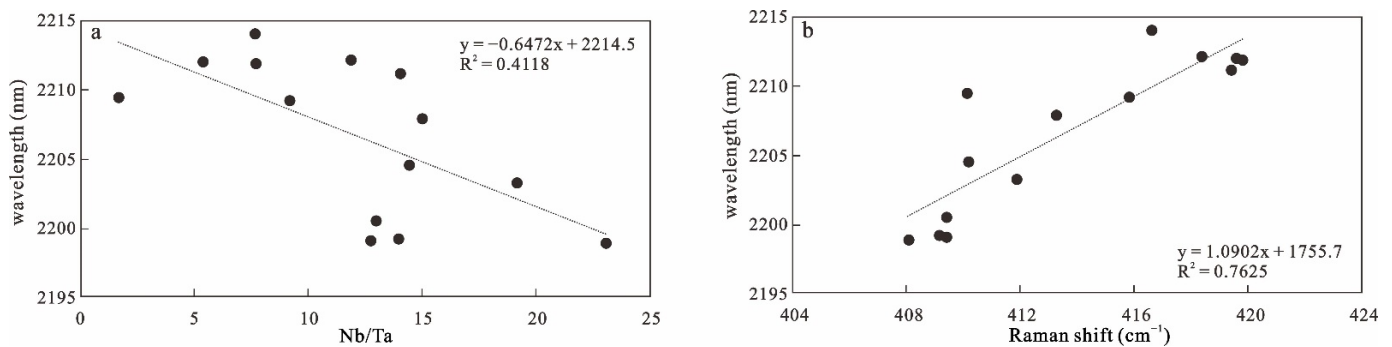


Figure 8. Binary diagram of the SWIR spectra (Pos 2200) for the Shimensi white mica vs. (a) Nb/Ta; (b) Raman shift (Al, O (br)).

5.1.2. Relationship between the SWIR Spectra and Micro-Raman Spectra of White Micas

According to the results described above, white micas from ore-bearing intrusions and barren intrusions show different SWIR and micro-Raman spectral features. For the ore-bearing intrusions, the shift of Pos2200 in white micas were biased towards the high wavelength direction, and the Raman shift of aluminium atom bridge-bonds (Al, O (br)) were also located at 410–420 cm⁻¹. For the barren intrusions, the shift of Pos2200 in white micas were biased towards the low wavelength direction, and the Raman shift of aluminium atom bridge-bonds (Al, O (br)) was mainly located between 406 and 413 cm⁻¹. According to the results of correlation analyses, there was a positive correlation between Pos2200 value in white mica and the Raman shift of aluminium atom bridge-bonds (Al, O (br)) in white mica, and the correlation was strong (Figure 8b). The shift of characteristic peak positions of SWIR spectra and Raman spectra is closely related to the displacement of elements. According to the statistical analysis, in this study area, the shift of Pos2200 in white micas have a more obvious response to whether the rock mass contains scheelite.

5.2. Indicative Significance of the SWIR Characteristics of White Mica Shimensi Porphyry Tungsten Deposits

According to the data, Tschermak substitution reaction ($\text{Al}^{\text{VI}}\text{Al}^{\text{IV}} \leftrightarrow (\text{Mg,Fe})^{\text{VI}}\text{Si}^{\text{IV}}$) will cause the shift of white mica Al-O-H absorption feature wavelength positions, and the possible factors causing Tschermak substitutions and thus the shift of Al-O-H absorption feature wavelength positions in white mica are lower-level erosion, including water, silicon, and aluminium activities, pH, redox conditions, temperature, and pressure [1,10,14,36–39]. Temperature affects the Tschermak substitution reaction, and at high temperatures, it will lead to an increase in the Al^{VI} content of white mica and a corresponding decrease in Mg and Fe. That is, the lower the Al-O-H wavelength, the higher the alteration temperature [1,36]. In considering the influence of pressure, phengite is often used as a geological pressure gauge. The higher the silicon content, the higher the pressure [37,38]. The pH value also affects the shift of Pos2200 in white mica. A low wavelength indicates strongly acidic conditions, and a high wavelength indicates a relatively neutral environment [14,39]. It is easy to form high wavelength white mica under oxidizing conditions [10].

Due to the different metallogenic environments and conditions found for different types of deposits, the features of the Pos2200 shift of white mica from the metallogenic area were also different. The Al-O-H absorption peak for white mica, which was closely

related to orebodies (mineralization) in volcanogenic massive sulphide (VMS) deposits, was located at a low wavelength and was generally characterized by high Al levels. This was mainly due to cold sea water that penetrated downwards through cracks in the volcano during formation of the VMS deposit sediment. With increasing depth, the seawater temperature increased and the pH decreased, so metal elements were leached from the host rock. Low wavelength white micas were formed at this high-temperature and in an acidic environment [40,41]. Laakso et al. (2016) found that in the Archean Izok Lake Zn-Cu-Pb-Ag VMS deposit, the Pos2200 value in white micas span a continuous wavelength range from 2194 to 2216 nm. In the drill core spectra, the white micas near the mineralized area have a low Al-O-H wavelength position [40]. The white mica near the porphyry deposit orebodies exhibited lower wavelength absorption peaks, which mainly indicates that the ore metal was more easily enriched and precipitated under acidic conditions [13,42]. In the porphyry system, the upwards migration of magmatic fluid was accompanied by a disproportionation reaction, the temperature gradually decreased, the acidity of the fluid increased, and Al-rich sericite minerals were formed in the shallow parts of the fluid migration channel. Generally, the shallow parts mostly contain Al-rich sericite (white mica), and the deep parts contain mostly phengite [39]. For example, in the Pebble porphyry copper-gold-molybdenum deposit, the highest gold and copper are coincident with the low Al-O-H wavelength associated with sericite alteration [13]. The epithermal hydrothermal deposits were closely related to porphyry deposits in space and were mainly enriched in paragonite and common muscovite, probably because their formation was closely related to acidic magmatic fluids and the formation pressure was low [43–45]. In the Trinity silver deposit, the Al-O-H wavelength of white micas range from 2196 nm to 2203 nm with proximity to mineralized zones [44]. For skarn deposits, phengite exhibiting a high wavelength peak is closely related to mineralization, which may be related to the temperature reduction and oxidizing conditions prevailing during mineralization, and the development of Fe and Mg rich carbonate rocks [45,46]. For example, in the Jiguanzui Cu-Au deposit, the Pos2200 of white micas have shifted toward higher wavelengths (>2209 nm) in the ore proximal area, Tian et al. think it may be caused by the substitution of Fe and Mg in the octahedral Al site. Additionally, in the Olympic Dam IOCG deposit, the Pos2200 value of white micas varied from 2213 nm distal to the mineralized zone to 2206 nm proximal to the mineralized zones [47].

In the Shimensi porphyry tungsten deposit, mineralization mainly depends on Yanshanian magma intrusion into Jinningian biotite granodiorite, and full contact with Jinningian pluton and undergoes strong water–rock reactions. The calcium-rich plagioclase in Jinningian pluton has decomposed and released a large amount of Ca^{2+} into the hydrothermal fluids, which is combined with $[\text{WO}_4]^{2-}$ and precipitated into scheelite along with the increase of fluid pH and the decrease of temperature [20,48]. As the fluid pH increased, the environment changed from acidic to relatively neutral, and the temperature decreased, resulting in more Al being replaced by Si, Fe, and Mg in the Tschermak substitution reaction. Thus, Al-O-H absorption feature wavelength position is inclined to the direction of a high wavelength. The white mica with Al-O-H absorption feature wavelength positions biased towards the high wavelength indicates the location of the ore-bearing intrusions. Therefore, hydrothermal white mica with a high Al-O-H wavelength is associated with scheelite mineralization in ore-bearing intrusions. In the barren intrusions, magmatic white mica with a low Al-O-H wavelength is more developed.

6. Conclusions

In this study, we analysed the SWIR, Raman spectra, petrographic characteristics, and geochemical elements of white mica in ore-bearing intrusions and the barren intrusions of the Shimensi mine of the Dahutang. The results show that white mica is prevalent in the Shimensi mine. White mica has different characteristics for different intrusions of the deposit and is closely related to mineralization. From the perspective of geochemical characteristics, white mica from the ore-bearing intrusions is characterized by high Si, Fe,

and Mg contents, low Al, Na, and K contents, and a low Nb/Ta ratio. From the perspective of SWIR characteristics, the white mica from the ore-bearing intrusions is mainly phengite (Pos 2200 > 2209 nm), which is consistent with the characteristics of high Si, Fe, Mg, and low Al. Its Raman spectrum also indicates high silicon content. The Raman shift of aluminium atom bridge-bonds (Al, O (br)) for white mica is mainly located between 410–420 cm^{-1} . In contrast, white mica from the barren intrusions shows a SWIR absorption peak located towards the low wavelength direction (Pos2200 < 2209 nm) with high Al, Na, K, Nb/Ta, and low Si, Fe, Mg, and the Raman shift of aluminium atom bridge-bonds (Al, O (br)) was mainly between 406–413 cm^{-1} . Moreover, the study shows that the Pos2200 in white mica is correlated with the Raman spectra and geochemical characteristics. In the process of scheelite mineralization, water–rock reaction occurs with the increase of fluid pH and the decrease of temperature, resulting in the formation of phengite with high Si, Fe, Mg, and low Al. So, the SWIR features of white mica can be used as an indicator for the exploration of the deposit. In addition, compared with the Raman spectra and geochemical analysis, the SWIR spectra measurement is more convenient and faster. The portable handheld SWIR spectrometer can directly measure the samples on the spot, and the measurement data can be obtained in a few seconds without damage to the samples. Therefore, application of the SWIR spectral features of white mica is of great significance for the exploration of porphyry tungsten deposits.

Author Contributions: Conceptualization, Z.Z. and J.D.; methodology, Z.Z. and J.D.; software, Z.Z., J.D., and M.F.; validation, Z.Z. and J.D.; formal analysis, Z.Z., J.D., and M.F.; investigation, Z.Z., J.D., X.W. (Xianguang Wang), Z.H., X.W. (Xin Wan), B.P., and M.F.; resources, J.D., X.W. (Xianguang Wang), Z.H., and X.W. (Xin Wan); data curation, Z.Z., J.D., and M.F.; writing—original draft preparation, Z.Z.; writing—review and editing, Z.Z. and J.D.; visualization, Z.Z. and J.D.; supervision, J.D., X.W. (Xianguang Wang), Z.H., X.W. (Xin Wan), and B.P.; project administration, Z.Z., J.D., X.W. (Xianguang Wang), Z.H., X.W. (Xin Wan), and B.P.; funding acquisition, X.W. (Xianguang Wang), Z.H., X.W. (Xin Wan), and B.P. All authors have read and agreed to the published version of the manuscript.

Funding: This work was financially supported by the General program of the National Natural Science Foundation of China (42172332), the Special fund for basic scientific research business expenses of central public welfare research institutes (KK2102, KK2017), the cultivation plan for backup projects of the national science and technology Award of Jiangxi Provincial Department of Science and Technology (2020) (20203AEI91004), the National Key Research and Development Program of China (2022YFC2905001), and the China Geological Survey Project (DD20221684).

Data Availability Statement: Data is contained within the article.

Acknowledgments: The authors would like to thank anonymous reviewers and academic editors for their constructive comments, which greatly improved the manuscript.

Conflicts of Interest: The authors declare no conflict of interest.

References

1. Duke, E.F. Near infrared spectra of muscovite, Tschermak substitution, and metamorphic reaction progress: Implications for remote sensing. *Geology* **1994**, *22*, 621. [[CrossRef](#)]
2. Zhao, Z.H.; Yan, S. Minerals and relevant metallogeny and exploration. *Acta Petrol. Sin.* **2019**, *35*, 31–68. (In Chinese with English abstract)
3. Chukanov, N.V.; Shendrik, R.Y.; Viskasina, M.F.; Pekov, I.V.; Sapozhnikov, A.N.; Shcherbakov, V.D.; Varlamov, D.A. Crystal chemistry, isomorphism, and thermal conversions of extra-framework components in sodalite-group minerals. *Minerals* **2022**, *12*, 887. [[CrossRef](#)]
4. Hamilton, V.E.; Christensen, P.R. Determining the modal mineralogy of mafic and ultramafic igneous rocks using thermal emission spectroscopy. *J. Geophys. Res.* **2000**, *105*, 9717–9733. [[CrossRef](#)]
5. Carrino, T.A.; Crósta, A.P.; Toledo, C.L.B.; Silva, A.M. Unveiling the hydrothermal mineralogy of the Chapi Chiara gold prospect, Peru, through reflectance spectroscopy, geochemical and petrographic data. *Ore Geol. Rev.* **2015**, *64*, 299–315. [[CrossRef](#)]
6. Lampinen, H.M.; Laukamp, C.; Occhipinti, S.A.; Hardy, L. Mineral footprints of the Paleoproterozoic sediment-hosted Abra Pb-Zn-Cu-Au deposit Capricorn Orogen, Western Australia. *Ore Geol. Rev.* **2019**, *104*, 436–461. [[CrossRef](#)]
7. Laukamp, C.; LeGras, M.; Montenegro, V.; Windle, S.; McFarlane, A. Grandite-based resource characterization of the skarn-hosted Cu-Zn-Mo deposit of Antamina, Peru. *Miner. Depos.* **2021**, *57*, 107–128. [[CrossRef](#)]

8. Ramakrishnan, D.; Bharti, R. Hyperspectral remote sensing and geological applications. *Curr. Sci.* **2015**, *108*, 879–891.
9. Dai, J.J.; Zhao, L.X.; Jiang, Q.; Wang, H.Y.; Liu, T.Y. Review of thermal-infrared spectroscopy applied in geological ore exploration. *Acta Geol. Sin.* **2020**, *94*, 2520–2533. (In Chinese with English abstract)
10. Wang, R.; Cudahy, T.; Laukamp, C.; Walshe, J.L.; Bath, A.; Mei, Y.; Young, C.; Roache, T.J.; Jenkins, A.; Roberts, M.; et al. White mica as a hyperspectral tool in exploration for the sunrise dam and Kanowna belle gold deposits, Western Australia. *Econ. Geol.* **2017**, *112*, 1153–1176. [[CrossRef](#)]
11. Lypaczewski, P.; Rivard, B.; Gaillard, N.; Perrouy, S.; Piette-Lauzière, N.; Bérubé, C.L.; Linnen, R.L. Using hyperspectral imaging to vector towards mineralization at the Canadian Malartic gold deposit, Québec, Canada. *Ore Geol. Rev.* **2019**, *111*, 102945. [[CrossRef](#)]
12. Xiao, B.; Chu, G.B.; Feng, Y.Z. Short-wave infrared (SWIR) spectral and geochemical characteristics of hydrothermal alteration minerals in the Laowangou Au deposit: Implications for ore genesis and vectoring. *Ore Geol. Rev.* **2021**, *139*, 104463. [[CrossRef](#)]
13. Harraden, C.L.; McNulty, B.A.; Gregory, M.J.; Lang, J.R. Shortwave infrared spectral analysis of hydrothermal alteration associated with the Pebble porphyry copper-gold-molybdenum deposit, Iliamna, Alaska. *Econ. Geol.* **2013**, *108*, 483–494. [[CrossRef](#)]
14. Zhou, Y.; Li, L.M.; Yang, K.; Xing, G.F.; Xiao, W.J.; Zhang, H.L.; Xiu, L.C.; Yao, Z.Y.; Xie, Z.J. Hydrothermal alteration characteristics of the Chating Cu-Au deposit in Xuancheng City, Anhui Province, China: Significance of sericite alteration for Cu-Au exploration. *Ore Geol. Rev.* **2020**, *127*, 103844. [[CrossRef](#)]
15. Liu, J.; Li, W.C.; Zhou, Q.; Yang, F.C.; Jiang, X.J.; Zhang, S.Z.; Guo, X.R. Advances in the study of porphyry tungsten deposits. *Geol. China* **2021**, *48*, 732–748. (In Chinese with English abstract)
16. Xiang, X.K.; Wang, P.; Zhan, G.N.; Sun, D.M.; Zhong, B.; Qian, Z.Y.; Tan, R. Geological characteristics of Shimensi tungsten polymetallic deposit in northern Jiangxi Province. *Miner. Depos.* **2013**, *32*, 1171–1187. (In Chinese with English abstract)
17. Fan, X.K.; Zhang, Z.Y.; Hou, Z.Q.; Mavrogenes, J.; Pan, X.F.; Zhang, X.; Dai, J.L.; Wu, X.Y. Magmatic processes recorded in plagioclase and the geodynamic implications in the giant Shimensi W–Cu–Mo deposit, Dahutang ore field, South China. *J. Asian Earth Sci.* **2021**, *212*, 104734. [[CrossRef](#)]
18. Gong, X.D. *Ore-Forming Fluid Evolution and Ore Genesis of the Dahutang Tungsten Polymetallic Ore Field in Jiangxi Province, China*; China University of Geosciences: Beijing, China, 2015. (In Chinese with English abstract)
19. Zhang, Z.; Deng, Y.F.; Yao, J.M.; Zong, J.Y.; Chen, H.Y. An array based seismic image on the Dahutang deposit, South China: Insight into the mineralization. *Phys. Earth Planet. Inter.* **2021**, *310*, 106617. [[CrossRef](#)]
20. Xu, G.F.; Li, Z.Y.; Yang, X.Y.; Liu, L. The role of Jiningian pluton in Yanshanian metallogenic events in the Dahutang tungsten deposit: Evidence from whole rock and zircon geochemistry. *Minerals* **2022**, *12*, 428. [[CrossRef](#)]
21. Fan, X.K.; Hou, Z.Q.; Zhang, Z.Y.; Mavrogenes, J.; Pan, X.F.; Zhang, X.; Xiang, X.K. Metallogenic ages and sulfur sources of the giant Dahutang W–Cu–Mo ore field, South China: Constraints from muscovite $^{40}\text{Ar}/^{39}\text{Ar}$ dating and in situ sulfur isotope analyses. *Ore Geol. Rev.* **2021**, *134*, 104141. [[CrossRef](#)]
22. Zhang, Z.Y.; Hou, Z.Q.; Peng, H.M.; Fan, X.K.; Wu, X.Y.; Dai, J.L. In situ oxygen isotope, trace element, and fluid inclusion evidence for a primary magmatic fluid origin for the shell-shaped pegmatoid zone within the giant Dahutang tungsten deposit, Jiangxi Province, South China. *Ore Geol. Rev.* **2019**, *104*, 540–560. [[CrossRef](#)]
23. Li, X.Y.; Zhang, J.R.; Lai, C.K. Comparison of magma oxygen fugacity and zircon Hf isotopes between Xianglushan tungsten-bearing granite and late Yanshanian granites in Jiangxi Province, South China. *Minerals* **2020**, *10*, 106. [[CrossRef](#)]
24. Wei, W.F.; Yan, B.; Shen, N.P.; Liu, L.; Zhang, Y.; Xiang, X.K. Muscovite $^{40}\text{Ar}/^{39}\text{Ar}$ age and H–O–S isotopes of the Shimensi tungsten deposit (northern Jiangxi Province, South China) and their metallogenic implications. *Minerals* **2017**, *7*, 162. [[CrossRef](#)]
25. Fan, X.K.; Mavrogenes, J.; Hou, Z.Q.; Zhang, Z.Y.; Wu, X.Y.; Dai, J.L. Petrogenesis and metallogenic significance of multistage granites in Shimensi tungsten polymetallic deposit, Dahutang giant ore field, South China. *Lithos* **2019**, *336–337*, 326–344. [[CrossRef](#)]
26. Peng, H.M.; Yuan, Q.; Li, Q.Y.; Liu, F.J.; Zhang, B.X.; Dan, X.H.; Zhang, Z.S.; Dong, X.F. Ore-controlling role of porphyreous biotite granite in Shimensi tungsten deposit and its prospecting significance. *Sci. Technol. Eng.* **2016**, *16*, 135–142. (In Chinese with English abstract)
27. Mao, J.W.; Wu, S.H.; Song, S.W.; Dai, P.; Xie, G.Q.; Su, Q.W.; Liu, P.; Wang, X.G.; Yu, Z.Z.; Chen, X.Y.; et al. The world-class Jiangnan tungsten belt: Geological characteristics, metallogeny, and ore deposit model. *Chin. Sci. Bull.* **2020**, *65*, 3746–3762. (In Chinese with English abstract). [[CrossRef](#)]
28. Reed, W.P. *Certificate of Analysis: Standard Reference Materials 610 and 611*; National Institute of Standards and Technology: Gaithersburg, MD, USA, 1992.
29. Liu, Y.S.; Hu, Z.C.; Gao, S.; Gunther, D.; Xu, J.; Gao, C.G.; Chen, H.H. In situ analysis of major and trace elements of anhydrous minerals by LA-ICP-MS without applying an internal standard. *Chem. Geol.* **2008**, *257*, 34–43. [[CrossRef](#)]
30. Mckeown, D.A.; Bell, M.I.; Edgar, S.E. Vibrational analysis of the dioctahedral mica: 2M1muscovite. *Am. Mineral.* **1999**, *84*, 1041–1048. [[CrossRef](#)]
31. Wang, A.; Freeman, J.J.; Jolliff, B.L. Understanding the Raman spectral features of phyllosilicates. *J. Raman Spectrosc.* **2015**, *46*, 829–845. [[CrossRef](#)]
32. Sulák, M.; Kaindl, R.; Putiš, M.; Sitek, J.; Krenn, K.; Tóth, I. Chemical and spectroscopic characteristics of potassium white micas related to polystage evolution of the Central Western Carpathians orogenic wedge. *Lithos* **2009**, *113*, 709–730. [[CrossRef](#)]

33. Zhou, Q.; Qin, K.; Tang, D.; Wang, C. A combined EMPA and LA-ICP-MS study of muscovite from pegmatites in the Chinese Altai, NW China: Implications for tracing rare-element mineralization type and ore-forming process. *Minerals* **2022**, *12*, 377. [[CrossRef](#)]
34. Volker, M.; Anthony, E.W. A hyperspectral study (V-NIR-SWIR) of the Nechalacho REE-Nb-Zr deposit, Canada. *J. Geochem. Explor.* **2018**, *188*, 194–215.
35. Carlos, A.; Graham, D.L. Raman spectroscopy coupled with reflectance spectroscopy as a tool for the characterization of key hydrothermal alteration minerals in epithermal Au–Ag systems: Utility and implications for mineral exploration. *Appl. Spectrosc.* **2021**, *75*, 1475–1496.
36. Herrmann, W.; Blake, M.; Doyle, M.; Huston, D.; Kamprad, J.; Merry, N.; Pontual, S. Short wavelength infrared (SWIR) spectral analysis of hydrothermal alteration zones associated with base metal sulfide deposits at rosebery and western Tharsis, Tasmania, and Highway-Reward, Queensland. *Econ. Geol.* **2001**, *96*, 939–955. [[CrossRef](#)]
37. Massonne, H.J.; Schreyer, W. Stability field of the high-pressure assemblage talc+ phengite and two new phengite barometers. *Eur. J. Mineral.* **1989**, *1*, 391–410. [[CrossRef](#)]
38. Massonne, H.J.; Szpurka, Z. Thermodynamic properties of white micas on the basis of high-pressure experiments in the systems K_2O -MgO- Al_2O_3 - SiO_2 - H_2O and K_2O -FeO- Al_2O_3 - SiO_2 - H_2O . *Lithos* **1997**, *41*, 229–250. [[CrossRef](#)]
39. Halley, S.; Dilles, J.H.; Tosdal, R.M. Footprints: Hydrothermal alteration and geochemical dispersion around porphyry copper deposits. *SEG Discov.* **2015**, *100*, 1–17. [[CrossRef](#)]
40. Laakso, K.; Peter, J.M.; Rivard, B.; White, H.P. Short-wave infrared spectral and geochemical characteristics of hydrothermal alteration at the Archean Izok Lake Zn-Cu-Pb-Ag volcanogenic massive sulfide deposit, Nunavut, Canada: Application in exploration target vectoring. *Econ. Geol.* **2016**, *111*, 1223–1239. [[CrossRef](#)]
41. Samani, P.; Prizomwala, S.P.; Rajawat, A.S. Assessing the mineral alteration in Ambaji–Deri region (northwestern India) using hyperspectral remote sensing. *J. Indian Soc. Remote Sens.* **2021**, *49*, 249–257. [[CrossRef](#)]
42. Xue, Q.W.; Wang, R.; Liu, S.Y.; Shi, W.X.; Tong, X.S.; Li, Y.Y.; Sun, F. Significance of chlorite hyperspectral and geochemical characteristics in exploration: A case study of the giant Qulong porphyry Cu-Mo deposit in collisional orogen, Southern Tibet. *Ore Geol. Rev.* **2021**, *134*, 104156. [[CrossRef](#)]
43. Squire, R.J.; Herrmann, W.; Pape, D.; Chalmers, D.I. Evolution of the Peak Hill high-sulfidation epithermal Au–Cu deposit, Eastern Australia. *Miner. Depos.* **2007**, *42*, 489–503. [[CrossRef](#)]
44. Kruse, F.A.; Bedell, R.L.; Taranik, J.V.; Peppin, W.A.; Weatherbee, O.; Calvin, W.M. Mapping alteration minerals at prospect, outcrop and drill core scales using imaging spectrometry. *Int. J. Remote Sens.* **2012**, *33*, 1780–1798. [[CrossRef](#)] [[PubMed](#)]
45. Mars, J.C. Mineral and lithologic mapping capability of WorldView 3 data at mountain Pass, California, Using true- and false-color composite images, band ratios, and logical operator algorithms. *Econ. Geol.* **2018**, *113*, 1587–1601. [[CrossRef](#)]
46. Tian, J.; Zhang, Y.; Cheng, J.M.; Sun, S.Q.; Zhao, Y.J. Short wavelength infra-red (SWIR) characteristics of hydrothermal alteration minerals in skarn deposits: Example from the Jiguanzui Cu–Au deposit, Eastern China. *Ore Geol. Rev.* **2019**, *106*, 134–149. [[CrossRef](#)]
47. Tappert, M.C.; Rivard, B.; Giles, D.; Tappert, R.; Mauger, A. The mineral chemistry, near-infrared, and mid-infrared reflectance spectroscopy of phengite from the Olympic Dam IOCG deposit, South Australia. *Ore Geol. Rev.* **2013**, *53*, 26–38. [[CrossRef](#)]
48. Li, H.W.; Zhao, Z.; Chen, Z.Y.; Guo, N.X.; Gan, J.W.; Li, X.W.; Yin, Z. Genetic relationship between the two-period magmatism and W mineralization in the Dahutang ore-field, Jiangxi Province: Evidence from zircon geochemistry. *Acta Petrol. Sin.* **2021**, *5*, 1508–1530. (In Chinese with English abstract)

Disclaimer/Publisher’s Note: The statements, opinions and data contained in all publications are solely those of the individual author(s) and contributor(s) and not of MDPI and/or the editor(s). MDPI and/or the editor(s) disclaim responsibility for any injury to people or property resulting from any ideas, methods, instructions or products referred to in the content.